Development of a Bi-functional RH-Strain Flexible Sensor

Shuo Fang, Alessander Turcios, Xi Chen, and Ioana Voiculescu
The City College of New York, New York, NY, 10031

Bi-functional sensors capable of simultaneously detecting multiple physical stimuli are essential for next-generation wearable and intelligent sensing systems. However, most reported bi-functional sensors rely on the simple integration of independent sensing elements without intrinsic coupling. In this work, a bi-functional sensing device for simultaneous relative humidity (RH) and mechanical strain detection was developed and systematically investigated. The system integrated a silk fibroin (SF)-based RH sensor and a carbon nanotube (CNT)–PDMS-based strain sensor. The two sensing units were then electrically coupled using both parallel and series configurations. Their impedance responses were studied through MATLAB simulation and experimental measurements under controlled RH and strain conditions. The results proved that the sensor could simultaneously measure RH and strain, but the measurable range has limitations. This work provides insights into the design and optimization of multifunctional sensing systems with coupled electrical responses.

I. Introduction

A bifunctional sensor is a sensor that is capable of simultaneously detecting two physical quantities. Among them, temperature–pressure sensors are the most widely studied [1, 2]. Many researchers have explored the integration of temperature and pressure sensing functions [3, 4], particularly in flexible devices for electronic skin applications. However, in most cases, these systems are simply combinations of two independent sensors, where the sensing mechanisms are not intrinsically coupled, and no signal decoupling is required. Temperature–pressure sensors, also known as tactile sensors, are increasingly applied in wearable systems [5] as well as in biomedical and healthcare applications [6].

Jung et al. presented a vertically stacked nanocellulose-based tactile sensor capable of simultaneously detecting pressure and temperature with minimal interference between pressure sensing and temperature sensing [7]. Zhang et al. demonstrated signal decoupling in a temperature–pressure sensor by analyzing current–voltage characteristics, where the slope of the curve corresponds to pressure and the intercept represents temperature [8].

Silk fibroin (SF), as a relative humidity (RH)-responsive material, was employed to design an RH sensor [9, 10]. An equivalent circuit model of the sensor was developed to understand how RH affects its electrical behavior. The feasibility of extending this system to a bifunctional RH–temperature sensor was also investigated. However, due to the

limited temperature range and the underlying mechanisms by which RH and temperature influence the resistance and capacitance of the material, temperature exhibits only a minor effect on the SF-based RH sensor. Consequently, the SF-based device is not suitable for simultaneous RH and temperature sensing [11].

In this paper, a bifunctional sensing system capable of simultaneously detecting RH and mechanical strain is developed and investigated. The study begins with the individual fabrication and characterization of an SF-based RH sensor and a CNT–PDMS-based strain sensor, demonstrating their selective sensitivity and minimal cross-interference. Based on their respective equivalent circuit models, the electrical behavior of each sensor is analyzed and used as the foundation for system-level integration.

Subsequently, the two sensors are coupled using both parallel and series connection modes to form an integrated sensing platform. The impedance responses of the coupled system are systematically studied through simulation and experimental measurements under controlled RH and strain conditions. The effects of electrical coupling, signal dominance, and parameter interaction are analyzed to evaluate the feasibility of simultaneous RH and strain detection. This chapter further discusses the limitations of each configuration and provides insight into decoupling strategies for multifunctional sensing systems.

II. Fabrication

The bi-functional strain-RH sensor was designed as an SF-based RH sensor embedded in a flexible strain sensor.

The SF-based RH sensor was fabricated by dropping one drop of SF solution on the surface of a commercial IDE substrate. Before coating, the IDE area was plasma-treated while the non-sensing area was covered with masking tape. After the treatment, the tape was removed, and one drop of SF solution was applied to the sensing area. The plasma treatment helped the SF solution spread evenly on the surface. Based on the sensing area and the concentration of the SF solution, the thickness of the SF film was estimated 0.8 μm. The detailed fabrication process was described in [9, 10].

The flexible strain sensor was fabricated using a CNT–PDMS composite. First, a mold with a serpentine pattern was fabricated via 3D printing. PDMS was prepared by mixing the base and curing agent at a 10:1 weight ratio and then poured into the mold. After curing, the PDMS was peeled from the mold, forming a serpentine microchannel that replicated the mold geometry. The channel was subsequently filled with a CNT–PDMS mixture containing 4 wt% CNT. In this way, the flexible strain sensor was successfully fabricated, as shown in Figure 1 (upper and middle).

The SF-based RH sensor was subsequently integrated onto the CNT–PDMS-based strain sensor. Two connection configurations were employed to couple the RH sensor and the strain sensor, namely the series connection mode and the parallel connection mode, as illustrated in Figure 1 (bottom).

The coupled sensor consists of two distinct regions: a strain application area and a non-strain area. Strain is applied exclusively to the strain application region, while no mechanical deformation is applied to the non-strain region, where the RH sensor is located.

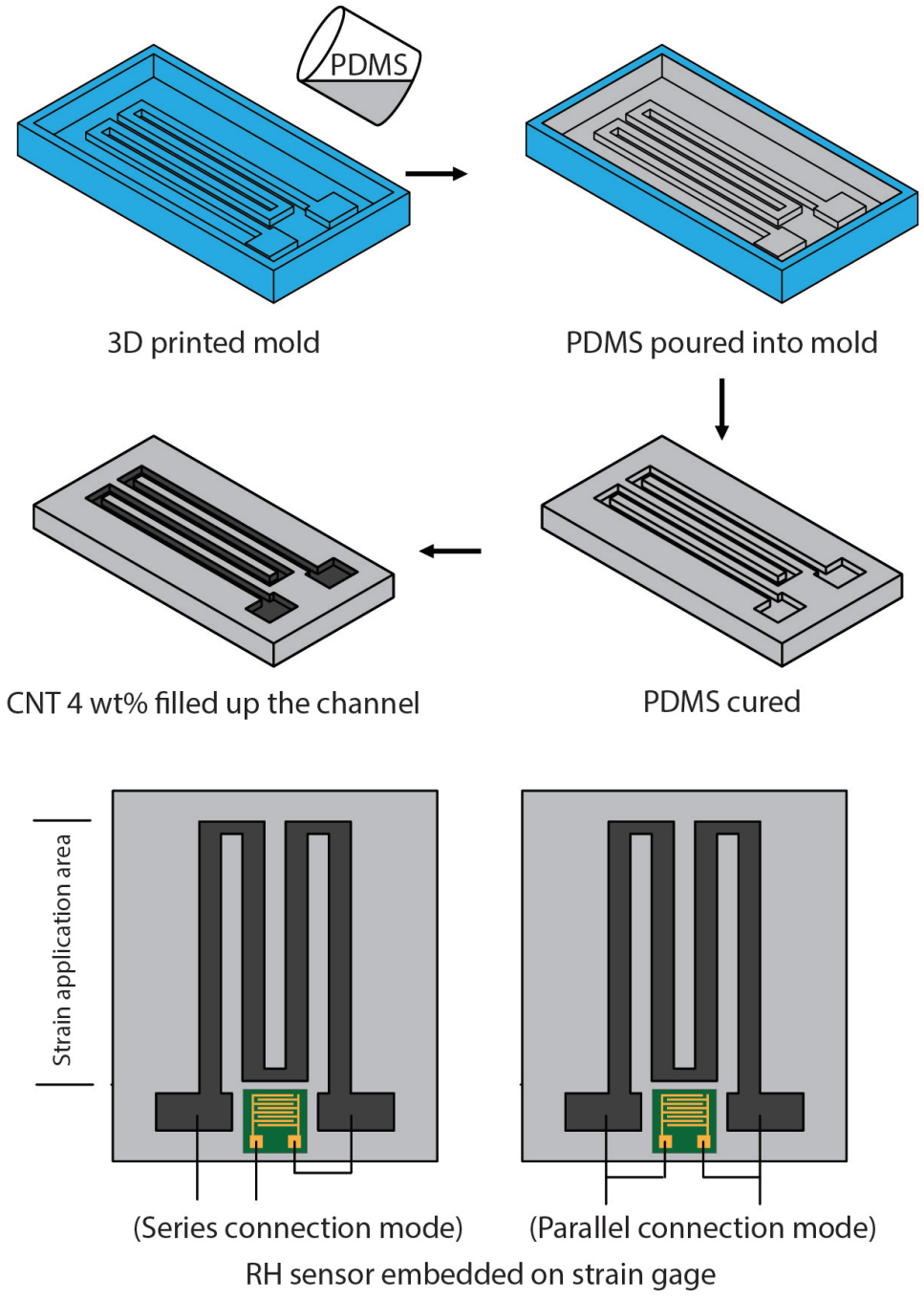

Fig. 1 The fabrication of the bi-functional flexible sensor.

III. RH sensor

The empty IDE was first characterized prior to the deposition of SF. The impedance of the empty IDE was measured. The result is illustrated in Figure 2. The impedance spectra under different RH levels overlap, indicating that the device is not significantly affected by RH. The measured impedance can be well fitted by an equivalent circuit model consisting of a resistor of 11 MΩ in parallel with a capacitor of 0.4 nF.

After depositing a 0.8 µm SF layer, the impedance was measured, as shown in Figure 3. The frequency was swept from 40 Hz to 1 MHz. As RH increases, the impedance decreases, and the peak in the phase plot shifts toward higher frequencies. The impedance spectra can be well described by a second-order equivalent circuit model, as introduced in [9, 10].

The impedance data were fitted to the equivalent circuit model, and the corresponding component values were extracted, as shown in Figure 4. R_1 represents the resistance of the SF material and decreases with increasing RH. C_1 corresponds to the capacitance of the SF material and increases with increasing RH. R_2 denotes the contact resistance between the SF layer and the IDE, which also decreases as RH increases. C_2 represents the intrinsic capacitance of the IDE and remains approximately constant.

IV. Strain sensor

The strain sensor, without embedding the RH sensor, was characterized by impedance measurements. The results are shown in Figure 5. In the plots, the line shape corresponds to strain, while the scatter color represents RH. It can be observed that strain has a significant effect on the impedance of the sensor. In contrast, RH shows no obvious influence on the strain sensor response.

The impedance data were fitted to an equivalent model of the strain sensor, as shown in Figure 6, which was established based on [12]. The component values were extracted and plotted as functions of RH and strain, as shown in Figure 7. The results indicate that RH has negligible influence on the component values, whereas strain exhibits a linear effect on them. These linear relationships between the component values and strain were further used in subsequent simulations.

V. Simulation of bi-functional sensor

From the previous section, it was demonstrated that the strain sensor is sensitive to strain but is not significantly affected by RH, whereas the RH sensor is rigid and insensitive to strain. The two sensors were then integrated using two different connection modes to form a coupled sensing system, and the performance for simultaneous detection of RH and strain was analyzed through MATLAB simulation.

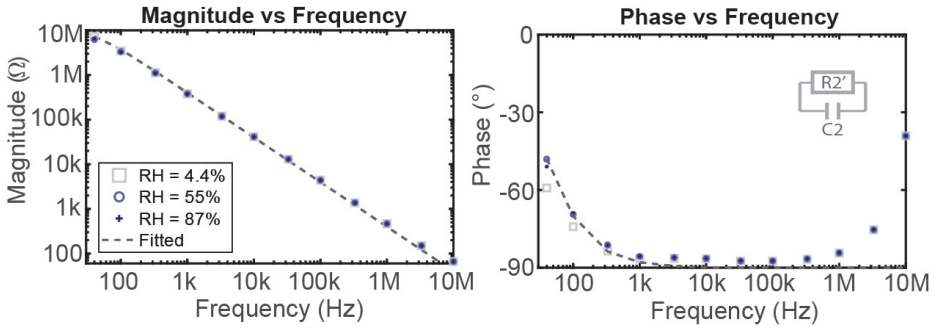

Fig. 2 The impedance of an empty IDE.

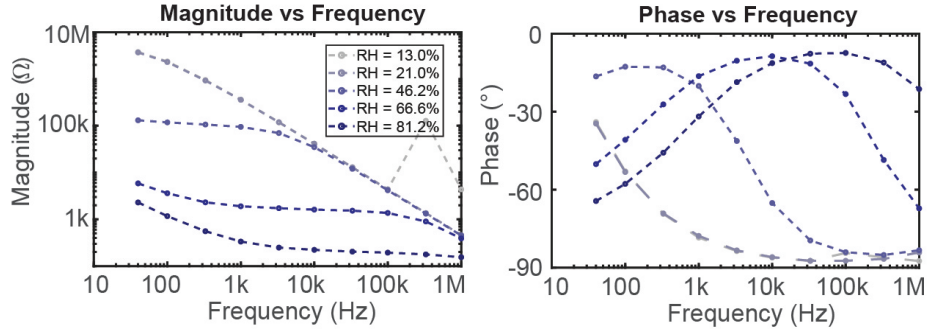

Fig. 3 The impedance of the RH sensor at different RH levels.

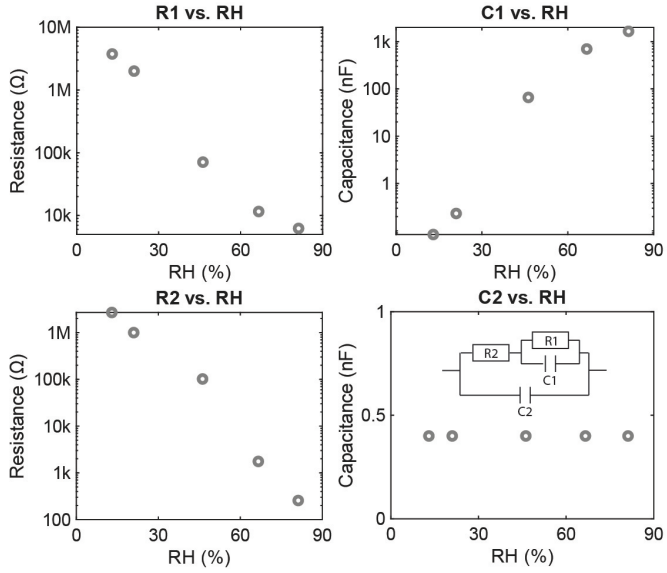

Fig. 4 The fitted value of components in the equivalent circuit.

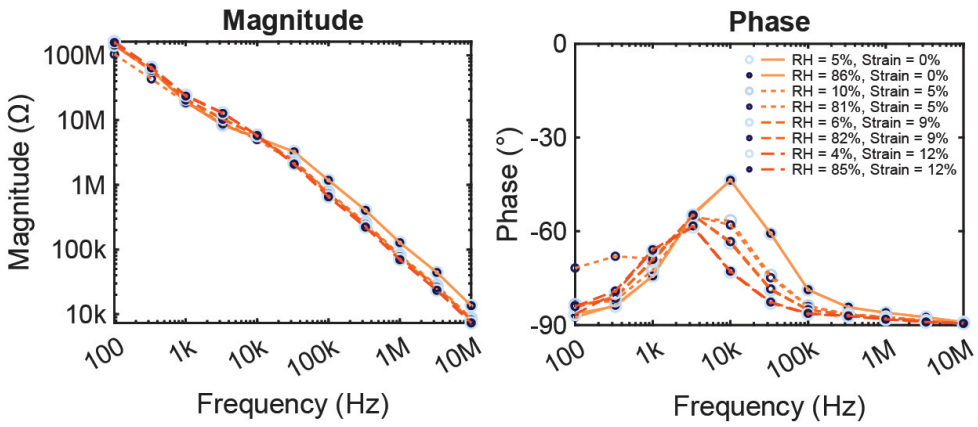

Fig. 5 The measured impedance of the strain sensor at different RH and strain conditions.

A. Parallel connection mode

The impedance of the coupled RH-strain sensor in the parallel connection mode was simulated at 1000 Hz. The impedance characteristics, including $-\mathrm{Im}(Z)$ vs. $\mathrm{Re}(Z)$ and phase vs. magnitude, are shown in Figure 8.

The zoomed-in $-\mathrm{Im}(Z)$ vs. $\mathrm{Re}(Z)$ plot at approximately 20% RH is shown below. The curves corresponding to different strain levels do not fully overlap but remain closely spaced, but the plots are located very close, since the impedance of the RH sensor is significantly lower than that of the strain sensor, and the RH sensor dominates the overall impedance response in the parallel configuration.

As RH increases, the separation between strain-dependent curves decreases, indicating reduced strain sensitivity. Similarly, increasing strain also leads to a reduction in sensitivity. When the strain exceeds a certain threshold, the curves shift downward and eventually overlap with other states, making it impossible to decouple RH and strain in this situation.

In summary, the simulated results demonstrate that the parallel-connected sensor is capable of simultaneously detecting RH and strain. However, the measurable strain range is limited from 0 to approximately 13%. In addition, higher RH levels reduce sensitivity and degrade measurement accuracy. It is therefore suggested that overall sensitivity can be improved by reducing the impedance of the strain sensor or increasing the impedance of the RH sensor.

B. Series connection mode

The impedance of the coupled RH-strain sensor in the series connection mode was simulated at 500 Hz, 1000 Hz, and 3300 Hz. The impedance characteristics, including $-\mathrm{Im}(Z)$ vs. $\mathrm{Re}(Z)$ and phase vs. magnitude, are shown in Figure 9.

In general, the scatter points in the plots occupy a well-defined region, where each point corresponds to a unique impedance value associated with a specific combination of RH and strain, enabling simultaneous sensing of both

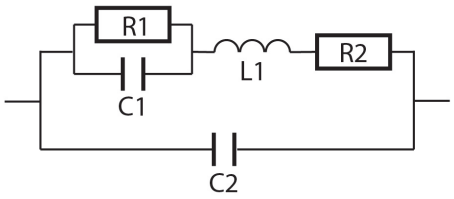

Fig. 6 The equivalent impedance model of the strain sensor.

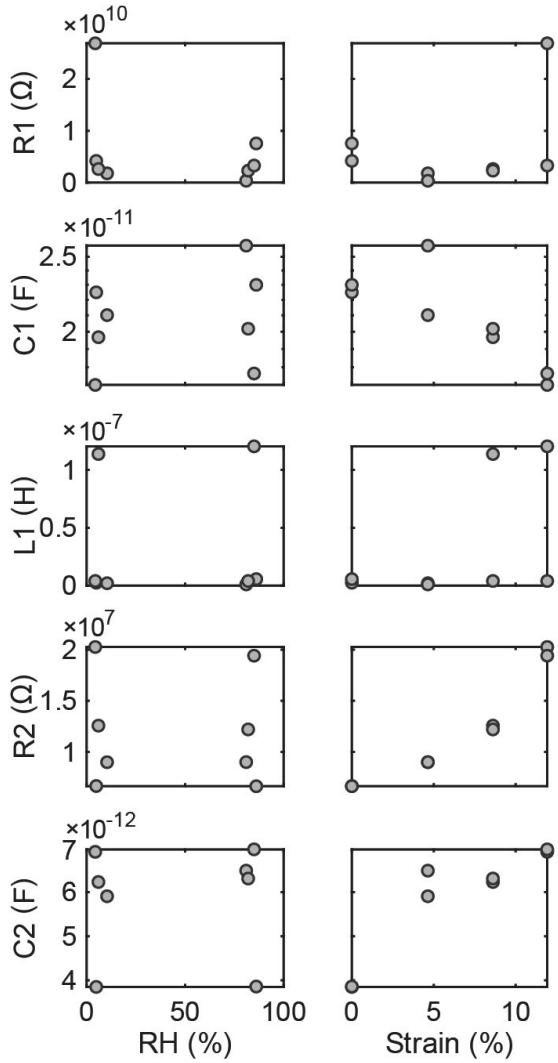

Fig. 7 The component values of the strain sensor in response to RH and strain.

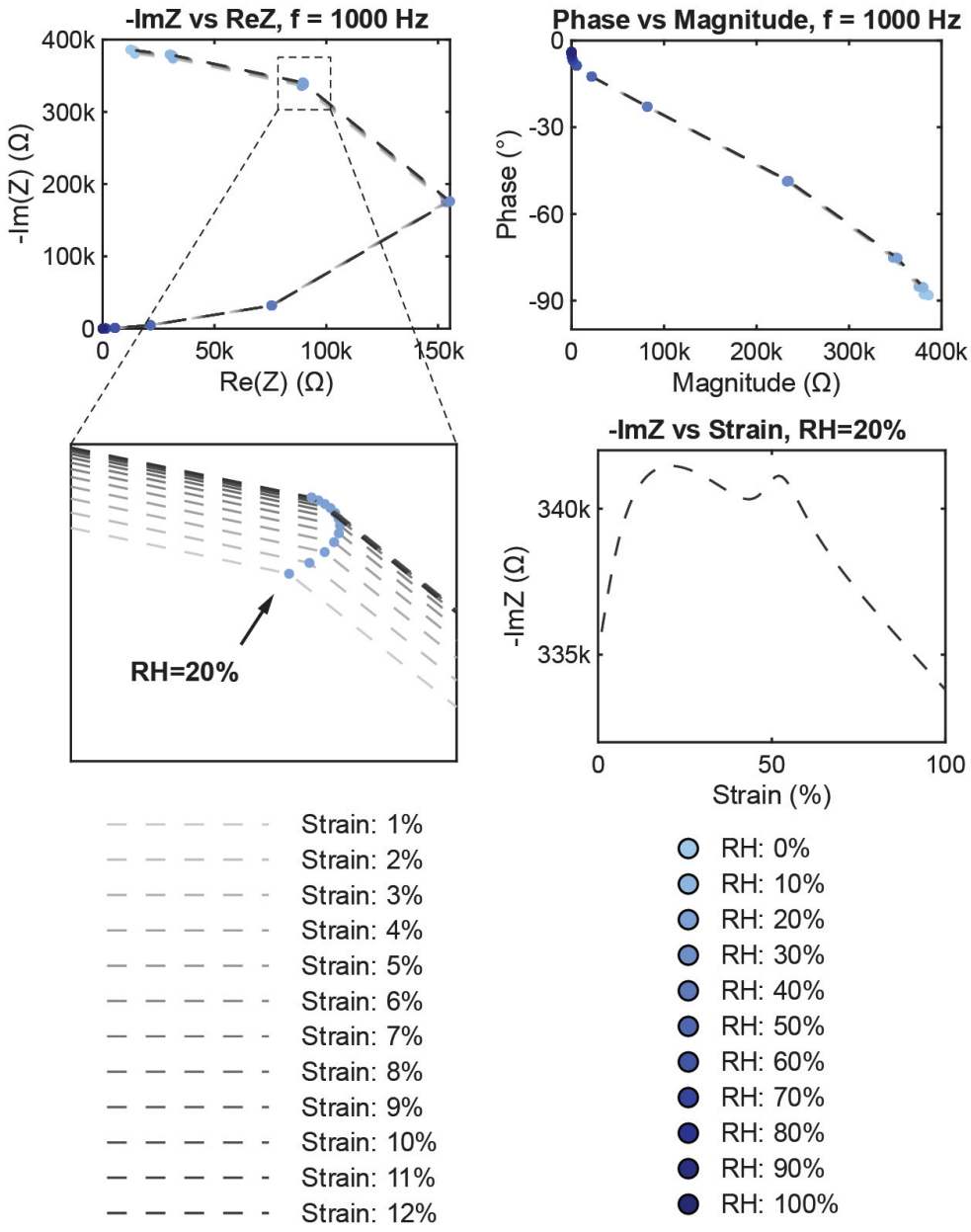

Fig. 8 MATLAB simulation of the impedance of the coupled RH–strain sensor in the parallel connection mode at 1000 Hz.

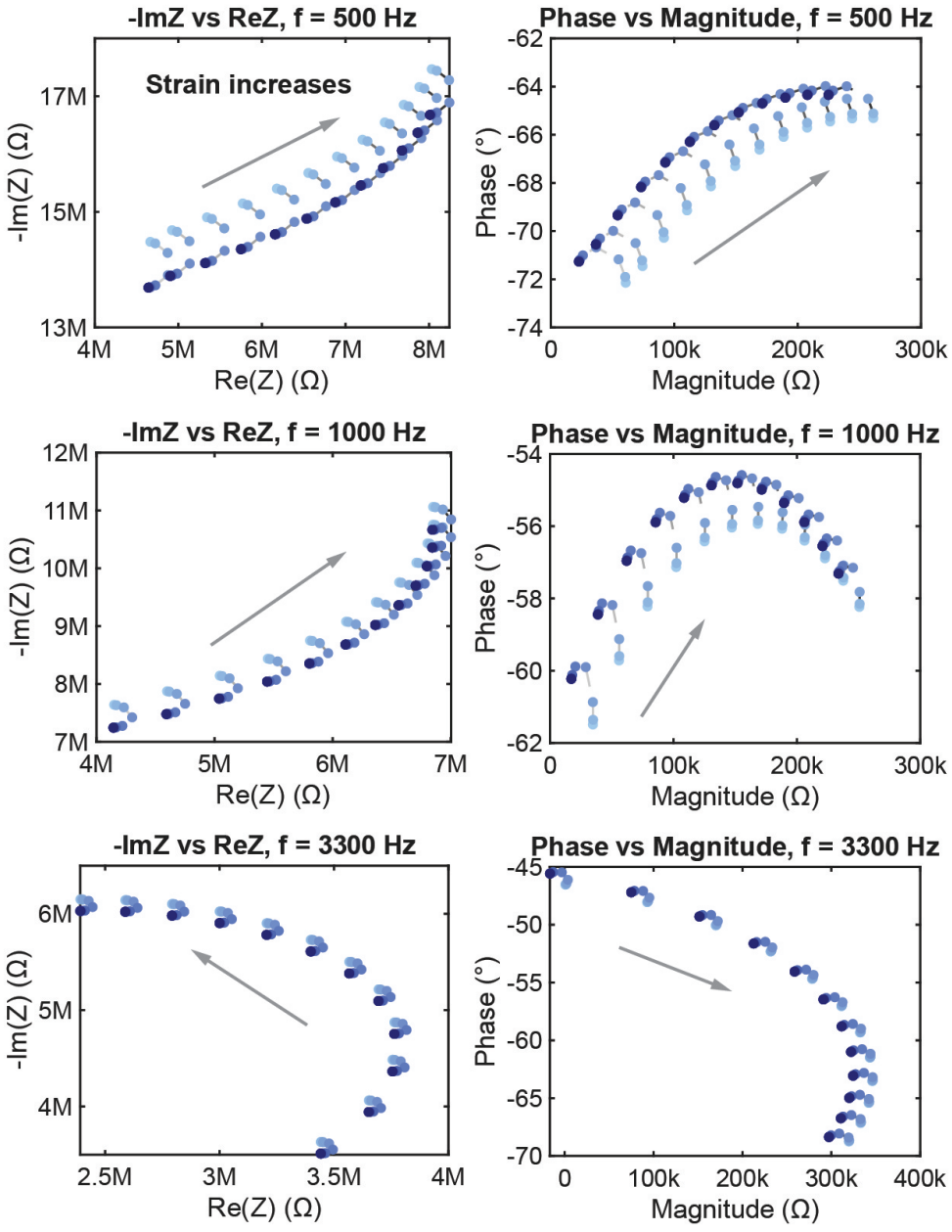

Fig. 9 MATLAB simulation of the impedance of the coupled RH–strain sensor in the series connection mode.

parameters.

However, at 500 Hz and 1000 Hz, the trajectories corresponding to different strain levels intersect as strain increases, leading to ambiguity in decoupling the measured values at the intersection regions. In contrast, at 3300 Hz, increased overlap occurs at low strain levels, making decoupling in these regions unreliable. At extremely high RH levels, the probability of overlap between different states further increases.

In summary, the simulated results indicate that the series-connected sensor can enable simultaneous RH and strain detection, but its performance is condition-dependent. At 500 Hz and 1000 Hz, the system performs well at low strain but degrades at high strain due to curve intersections. At 3300 Hz, the opposite trend is observed, with better performance at high strain but reduced accuracy at low strain. Additionally, under very high RH conditions, the sensitivity and sensing accuracy are significantly reduced.

VI. Experiment results of bi-functional sensor

Experiments were conducted on the bifunctional sensor in both parallel and series connection modes. Strain was applied to the strain application region using a 3D-printed stretching apparatus. The sensor was placed in a humidity-controlled chamber to regulate RH. During simultaneous application of strain and RH, the impedance was measured.

A. Parallel connection mode

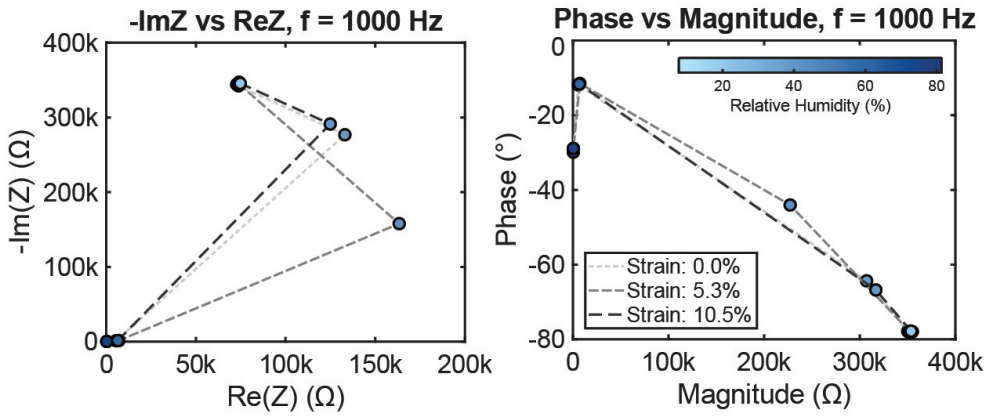

Fig. 10 Measured impedance of the coupled RH–strain sensor in the parallel connection mode at 1000 Hz.

Figure 10 shows the measured impedance characteristics at 1000 Hz for the parallel connection mode. Both the $-\mathrm{Im}(Z)$ vs. $\mathrm{Re}(Z)$ and phase vs. magnitude plots follow trajectories consistent with the simulated results in Figure 8. However, due to measurement noise and experimental uncertainties, the response exhibits RH-dominated behavior, and the strain effect cannot be reliably decoupled.

B. Series connection mode

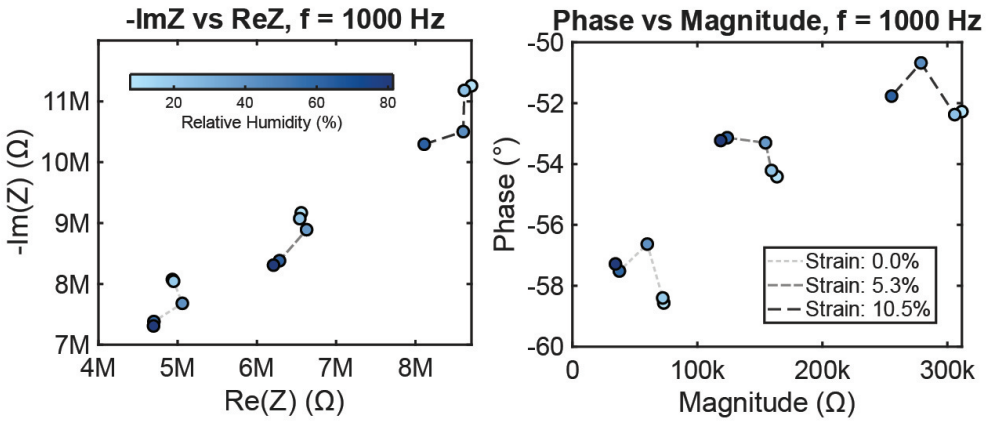

Fig. 11 Measured impedance of the coupled RH–strain sensor in the series connection mode at 1000 Hz.

Figure 11 shows the measured impedance characteristics at 1000 Hz for the series connection mode. Both the $-\mathrm{Im}(Z)$ vs. $\mathrm{Re}(Z)$ and phase vs. magnitude plots are presented. As strain increases, the corresponding data shift toward the upper-right region of the plots, resulting in a confined impedance region that enables bifunctional sensing, consistent with the simulation in Figure 9.

However, the reduced sensitivity at high RH levels limits measurement accuracy. In addition, potential intersections at higher strain levels may occur, which makes the sensor less suitable for high-strain sensing conditions.

VII. Conclusion

In this paper, a bifunctional sensing system integrating RH and strain sensors was developed and systematically investigated. The fabrication processes of both the SF-based RH sensor and the CNT–PDMS-based strain sensor were first presented. Individual characterization demonstrated that the RH sensor exhibits strong sensitivity to humidity while remaining insensitive to strain, whereas the strain sensor shows pronounced strain dependence with negligible influence from RH. These complementary properties provide the foundation for coupled sensing.

Based on the extracted equivalent circuit models, the performance of the coupled sensor was analyzed through simulations for both parallel and series connection modes. The simulation results revealed that the parallel configuration is dominated by the lower impedance RH sensor, enabling reliable RH sensing but limiting strain sensitivity and decoupling capability. In contrast, the series configuration provides a broader impedance distribution, allowing simultaneous sensing of RH and strain under certain conditions, although intersections in the impedance space may lead to ambiguity depending on frequency, strain level, and RH.

Experimental validation was then carried out for both connection modes. The measured results for the parallel configuration agreed with simulations, showing RH-dominated behavior with limited ability to resolve strain due to noise

and low sensitivity. For the series configuration, the measurements confirmed the feasibility of bifunctional sensing, with impedance responses occupying distinguishable regions corresponding to different RH and strain combinations. However, reduced sensitivity at high RH and potential overlap at higher strain levels impose limitations on sensing accuracy and operational range.

Overall, this work demonstrates the feasibility of integrating RH and strain sensing into a single device through electrical coupling. The results highlight the trade-offs between parallel and series configurations and emphasize the importance of impedance matching and operating conditions in achieving reliable decoupled sensing. Future improvements may focus on optimizing the relative impedance of the two sensors and selecting appropriate operating frequencies to enhance sensitivity and expand the usable sensing range.

References

[1] Lu, J., Yu, Y., Qin, S., Li, M., Bian, Q., Lu, Y., Hu, X., Yang, J., Meng, Z., and Zhang, Z., "High-performance temperature and pressure dual-parameter sensor based on a polymer-coated tapered optical fiber," *Optics Express*, Vol. 30, No. 6, 2022, pp. 9714–9726.

[2] Zhang, Z., Zhang, H., Zhang, Q., Zhao, X., Li, B., Zang, J., Zhao, X., and Zhang, T., "A pressure and temperature dual-parameter sensor based on a composite material for electronic wearable devices," *Micromachines*, Vol. 14, No. 3, 2023, p. 690.

[3] Wang, P., Yu, W., Li, G., Meng, C., and Guo, S., "Printable, flexible, breathable and sweatproof bifunctional sensors based on an all-nanofiber platform for fully decoupled pressure–temperature sensing application," *Chemical Engineering Journal*, Vol. 452, 2023, p. 139174.

[4] Liang, Y., Zhang, C., Mi, X., Ma, X., and Wang, J., "High-performance self-decoupling flexible pressure–temperature bifunctional sensors based on TPU/IL for electronic skin," *Composites Part A: Applied Science and Manufacturing*, Vol. 190, 2025, p. 108656.

[5] Jayathilaka, W. A. D. M., Qi, K., Qin, Y., Chinnappan, A., Serrano-García, W., Baskar, C., Wang, H., He, J., Cui, S., Thomas, S. W., et al., "Significance of nanomaterials in wearables: a review on wearable actuators and sensors," *Advanced Materials*, Vol. 31, No. 7, 2019, p. 1805921.

[6] Wang, Y., Yang, B., Hua, Z., Zhang, J., Guo, P., Hao, D., Gao, Y., and Huang, J., "Recent advancements in flexible and wearable sensors for biomedical and healthcare applications," *Journal of Physics D: Applied Physics*, Vol. 55, No. 13, 2022, p. 134001.

[7] Jung, M., Kim, K., Kim, B., Lee, K.-J., Kang, J.-W., and Jeon, S., "Vertically stacked nanocellulose tactile sensor," *Nanoscale*, Vol. 9, No. 44, 2017, pp. 17212–17219.

[8] Zhang, F., Zang, Y., Huang, D., Di, C.-a., and Zhu, D., "Flexible and self-powered temperature–pressure dual-parameter sensors using microstructure-frame-supported organic thermoelectric materials," *Nature communications*, Vol. 6, No. 1, 2015, p. 8356.

[9] Fang, S., Zhang, Y., Khan, M. K., Chen, X., and Voiculescu, I., "Study of the Equivalent Model of Silk Fibroin Based Relative Humidity Sensor," *ASME International Mechanical Engineering Congress and Exposition*, Vol. 89404, American Society of Mechanical Engineers, 2025, p. V009T14A007.

[10] Fang, S., Zhang, Y., Khan, M. K., Chen, X., and Voiculescu, I., "Ultra-fast silk-based humidity sensor enabled by water-induced impedance modulation," *Authorea Preprints*, 2025.

[11] Fang, S., Raoult, B., Chen, X., and Voiculescu, I., "Study of Temperature Affects on a Silk-Based Humidity Sensor," *Authorea Preprints*, 2025.

[12] Qian, C., Xiao, T., Chen, Y., Wang, N., Li, B., and Gao, Y., "3D printed reduced graphene oxide/elastomer resin composite with structural modulated sensitivity for flexible strain sensor," *Advanced Engineering Materials*, Vol. 24, No. 4, 2022, p. 2101068.